

Supporting information for

Hard ferromagnetism down to the thinnest limit of iron-intercalated tantalum disulfide

Samra Husremović,^a Catherine K. Groschner,^a Katherine Inzani,^{b,c,†} Isaac M. Craig,^a Karen C. Bustillo,^d Peter Ercius,^d Nathanael P. Kazmierczak,^{a,‡} Jacob Syndikus,^a Madeline Van Winkle,^a Shaul Aloni,^c Takashi Taniguchi,^e Kenji Watanabe,^f Sinéad M. Griffin,^{b,c} D. Kwabena Bediako^{a,g*}

^a *Department of Chemistry, University of California, Berkeley, California 94720, United States*

^b *Materials Sciences Division, Lawrence Berkeley National Laboratory, Berkeley, CA 94720, United States*

^c *The Molecular Foundry, Lawrence Berkeley National Laboratory, Berkeley, California 94720, United States*

^d *National Center for Electron Microscopy, Molecular Foundry, Lawrence Berkeley National Laboratory, Berkeley, California 94720, United States*

^e *Research Center for Functional Materials, National Institute for Materials Science, Tsukuba 305-0044, Japan*

^f *International Center for Materials Nanoarchitectonics, National Institute for Materials Science, Tsukuba 305-0044, Japan*

^g *Chemical Sciences Division, Lawrence Berkeley National Laboratory, Berkeley, California 94720, United States*

[†] *Current position: School of Chemistry, University of Nottingham, Nottingham, NG7 2RD, United Kingdom*

[‡] *Current position: Division of Chemistry and Chemical Engineering, California Institute of Technology, Pasadena, CA 91125, United States*

* *E-mail: bediako@berkeley.edu*

TABLE OF CONTENTS

<i>Hard ferromagnetism down to the thinnest limit of iron-intercalated tantalum disulfide</i>	1
1 SAMPLE PREPARATION	3
1.1 Mechanical exfoliation of hexagonal boron nitride (hBN)	3
1.2 Mechanical exfoliation of 2H-TaS ₂	3
1.3 Determination of layer numbers for 2H-TaS ₂ crystals	3
1.4 Encapsulation of 2H-TaS ₂ with hBN	5
1.4.1 Need for encapsulation.....	5
1.4.2 Details of encapsulation	5
1.5 Sample preparation for transmission electron microscopy (TEM)	6
1.5.1 Samples for imaging along the crystallographic <i>c</i> -axis.....	6
1.5.2 Cross-sectional samples for imaging along the <i>ab</i> -plane	6
2 CHEMICAL INTERCALATION	7
2.1 Methods for intercalation of zerovalent iron precursors.....	7
2.1.1 Method 1: Intercalation with Fe(CO) ₅ in toluene	7
2.1.2 Method 2: Intercalation with Fe(CO) ₅ in acetonitrile or acetone.....	8
2.2 Insights into the carbonyl intercalation chemistry	8
2.3 Nanofabrication.....	9
3 ELECTRON MICROSCOPY AND RAMAN SPECTROSCOPY	10
3.1 Transmission electron microscopy (TEM)	10
3.2 Results of high-resolution TEM (HRTEM) imaging.....	10
3.3 STEM-EDS analysis.....	11
3.4 Filtering of DPC-STEM micrographs	12
3.5 Analysis of the Fe trigonal distortion from DPC-STEM data	13
3.6 Analysis and results of electron energy loss spectroscopy (EELS)	14
3.7 Raman spectroscopy.....	15
4 MAGNETOTRANSPORT MEASUREMENTS	15
4.1 Symmetrization of magnetotransport data.....	15
4.2 Analysis of the ordinary Hall effect (OHE).....	16
4.3 Temperature dependence of hysteretic behavior in 2-, 3-, and 5- layer crystals.....	18
4.4 Magnetoresistance of the 5-, 3- and 2-layer crystals with $H \parallel c$ and $H \parallel ab$	20
4.6 Origin of the resistivity upturn for bilayer Fe _x TaS ₂	21
5 DETAILS OF THE THEORETICAL CALCULATIONS	21
6 DATA PROCESSING AND PRESENTATION	22
7 REFERENCES	23

1 SAMPLE PREPARATION

1.1 Mechanical exfoliation of hexagonal boron nitride (hBN)

The mechanical exfoliation of hBN (used as received from T. Taniguchi and K. Watanabe) is performed outside the glovebox. First, 90 nm SiO₂/Si chips are cut into ~1 × 1 cm pieces and cleaned for 60 minutes in an ozone cleaner. Immediately before the chip cleaning is complete, 4 hBN crystals (~1.5 mm × 1.5 mm) are tessellated with an adhesive tape (Magic Scotch). Then, the chips are taken out of the ozone cleaner, placed shiny-side-up onto the tape and pressed for 10 minutes with finger pressure. After this, the tape is swiftly taken off the chips.

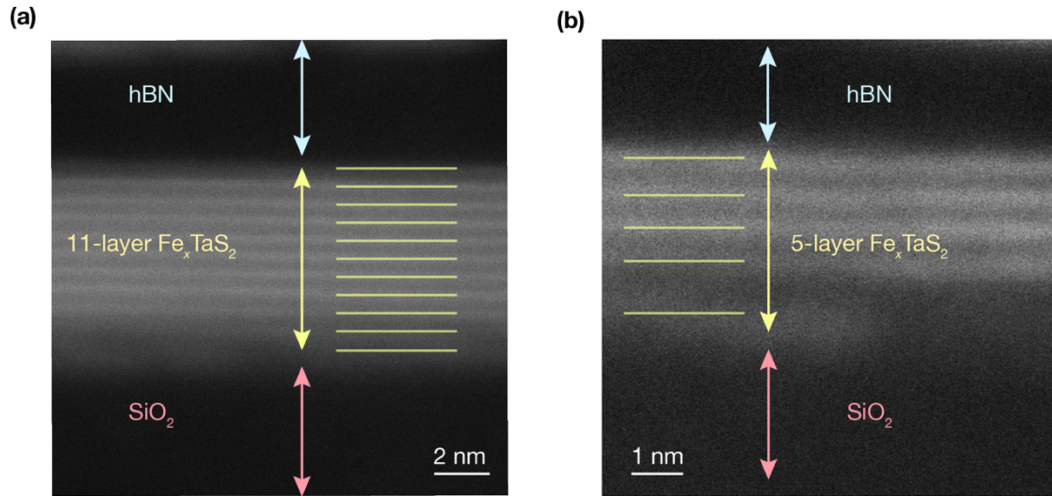
1.2 Mechanical exfoliation of 2H-TaS₂

The mechanical exfoliation of 2H-TaS₂ (HQ Graphene) is done in an Ar glovebox using an adhesive tape (Magic Scotch). First, 90 nm SiO₂/Si chips are cut into ~1 × 1 cm pieces and cleaned for 2 minutes in an oxygen plasma cleaner. The chips are left on the glovebox hotplate at 200 °C while tessellating a large 2H-TaS₂ crystal (~3 × 3 mm) with the adhesive tape. Then, the chips are taken off the hotplate, placed shiny-side-up onto the tape and pressed for 10 minutes with finger pressure. After this, the tape is swiftly taken off the chips.

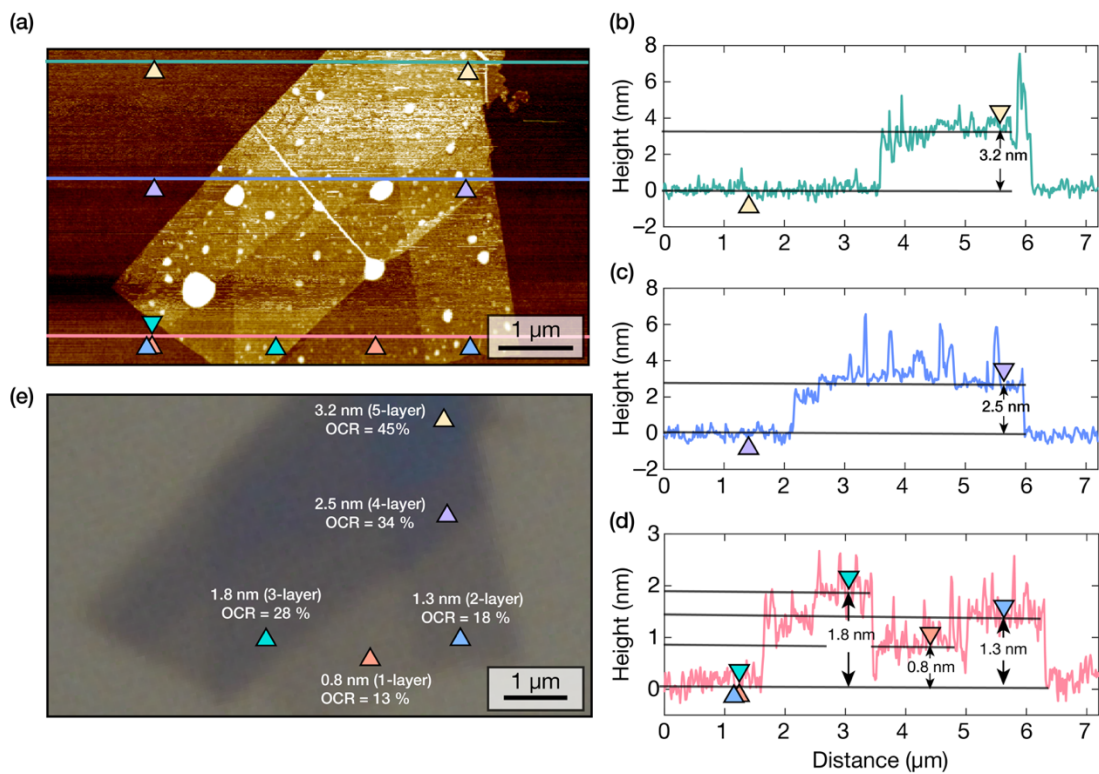
1.3 Determination of layer numbers for 2H-TaS₂ crystals

We determined the number of 2H-TaS₂ layer in thicker devices (≥ 5 -layers) by fabricating them into cross-sectional samples using focused ion beam (FIB) and examining them with high-resolution scanning transmission electron microscopy (STEM) (**SI Figure 1**). In HRSTEM, TaS₂ layers appear as bright lines, owing to the heavy Ta ions. Thus, the layers can be easily identified and counted.

For thin samples (< 6 layers) on 90 nm SiO₂/Si, we found that the thickness can be reliably identified using optical contrast measurements, which we related to thickness using atomic force microscopy (AFM) (**SI Figure 2**).¹



SI Figure 1. HRSTEM of a (a) 11-layer and (b) 5-layer sample encapsulated with hBN. The bright lines represent the TaS_2 layers, which are highlighted with yellow lines.

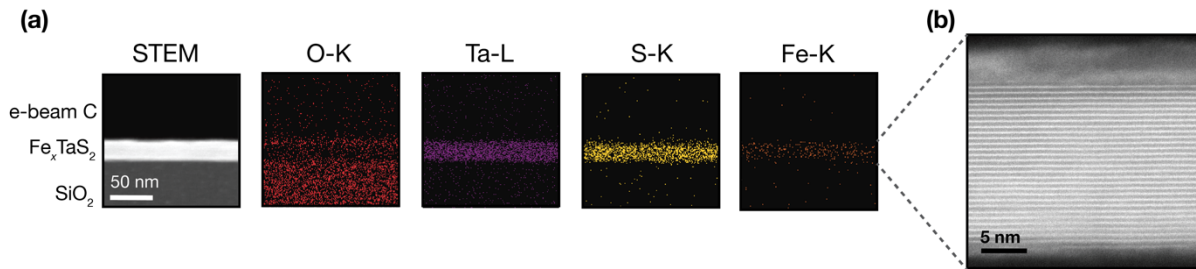


SI Figure 2. (a) Atomic force microscopy (AFM) image of a $2H\text{-TaS}_2$ flake encapsulated in thin hBN. Green, blue, and red lines are drawn where AFM height profiles were obtained. Height difference was obtained between points marked in equally colored triangles. (b), (c), (d) AFM height profiles along the green, blue, and red lines, respectively. The height differences between the equally colored triangular markers are labeled. (e) Optical image of the flake from (a) before encapsulation with hBN. For regions whose height was obtained in (b)–(d), red optical contrast (OCR) on 90 nm SiO_2/Si was calculated and labeled. The number of layers, also indicated in the figure, was inferred from the AFM-derived heights.

1.4 Encapsulation of 2H-TaS₂ with hBN

1.4.1 Need for encapsulation

The mechanically exfoliated 2H-TaS₂ needs to be encapsulated to prevent surface degradation. Signs of surface degradation of uncapped flakes were evident in cross-sectional STEM coupled with energy-dispersive X-ray spectroscopy (EDS). These studies confirmed that the entirety of our sample contains Fe, Ta, and S, as expected for Fe_xTaS₂ (SI Figure 3a). However, we also discovered the formation of an oxygen-rich (SI Figure 3a) and amorphous (SI Figure 3b) surface layer when samples were prepared without capping by hBN. Such an amorphous layer was not observed for hBN-capped flakes (SI Figure 1), indicating that hBN encapsulation is an effective method of protecting air-sensitive Fe_xTaS₂ flakes. All samples used in magnetotransport measurements were encapsulated with hBN (SI Figure 4).



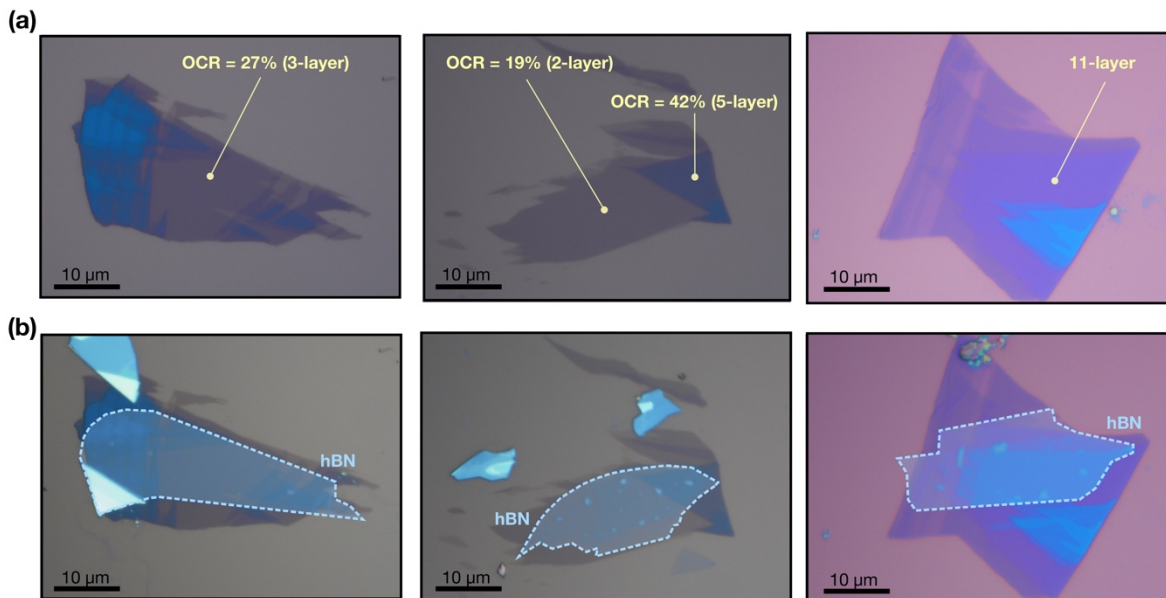
SI Figure 3. (b) Cross-sectional STEM-EDS maps of an uncapped Fe_xTaS₂ flake on SiO₂/Si after reaction and annealing. (b) HRSTEM image of the sample from (a).

1.4.2 Details of encapsulation

Our samples were prepared with the dry transfer method using a home-built micro-manipulation stage in an Ar glovebox.^{2,3} In a typical procedure, we prepared a polymeric stamp consisting of a poly(bisphenol A carbonate), PC, film covering a polydimethylsiloxane (PDMS) stamp on a glass slide. To assemble the polymer stamp, we first prepared a solution of PC by making a 5% w/w solution of PC (Sigma Aldrich) in chloroform (Lab Chem). The PC solution was placed onto a glass slide using a glass pipette and spread by sandwiching the PC-covered slide with a clean glass slide. The two slides were quickly separated and placed PC-side-up onto a hotplate at 120 °C. After 5 minutes of baking, a relatively uniform PC film was formed. This film was cut into small squares (2 mm × 2 mm) using a razor blade. The squares were placed onto a 4 mm × 4 mm PDMS square that has been attached to a glass slide. When this PC/PDMS stack was completed, it was placed on a hotplate at 120 °C for 2 minutes.

Next, the PC/PDMS polymer stamp was used to pick up hBN, which was subsequently placed onto a 2H-TaS₂ flake. The edges of the 2H-TaS₂ flake were left uncapped to enable subsequent intercalation. Next, the hBN was released on the 2H-TaS₂ flake by melting the PC stamp at 160 °C. For thicker 2H-TaS₂ flakes (> 6

layers), the PC film was dissolved in chloroform for 20 minutes under ambient atmosphere. The chip containing the sample was then subsequently washed with isopropanol (Sigma Aldrich) and dried with flowing N_2 . For thinner samples (< 6 layers), the PC film was dissolved in dichloromethane (Fisher Scientific) for 20 minutes in an Ar-filled glovebox. The sample was then rinsed in toluene and dried with flowing Ar.



SI Figure 4. (a) Optical micrographs of $2H-TaS_2$ flakes after mechanical exfoliation. Uniform flake areas, whose layer count is marked in yellow, were nanofabricated into devices. The red channel optical contrast (OCR) is indicated for flakes whose layer count was obtained with optical contrast measurements. **(b)** Flakes after encapsulation with hexagonal boron nitride (hBN). The hBN-covered flake areas are false-colored in light blue.

1.5 Sample preparation for transmission electron microscopy (TEM)

1.5.1 Samples for imaging along the crystallographic c -axis

TEM samples for imaging along the c -axis were prepared on silicon nitride holey TEM grids with a 200 nm membrane thickness (Norcada). The previously described dry transfer method was used to transfer $2H-TaS_2$ flakes from the SiO_2/Si support onto the silicon nitride membrane. Immediately before stacking, the TEM grid was cleaned for 5 minutes in an oxygen plasma cleaner.

1.5.2 Cross-sectional samples for imaging along the ab -plane

Cross-sectional TEM samples were prepared with FEI Helios 660 and Thermo Scientific Scios 2 focused ion beam scanning electron microscopy (FIB-SEM) systems. A 200 nm coating of Pt or C was deposited over the device's Hall bar channel using an electron beam at 5 kV and 1.6 nA. This was followed by a deposition of

2.5 μm Pt or C layer using a gallium-ion beam at 30 kV and 0.1 nA. The initial bulk-out was performed with a 30 kV Ga beam and 3 nA current, while the bulk-out cleaning was done with a 1 nA current. For the initial thinning, a 30 kV Ga beam was used, while the current was increasingly lowered as the sample became thinner. Initial thinning was started with a 1 nA current, while the final current for the rough thinning was typically 0.3 nA. After the sample was approximately 150 nm thick, we switched to the 5 kV and 40 pA settings. The final polishing was done at 2 kV and 40 pA to reduce the ion beam damage.

Note that sample damage occurs at the interfaces of Fe_xTaS_2 with other layers, including SiO_2 and hBN. This was evident from HRSTEM, where Fe_xTaS_2 layers at interfaces look deformed and blurred (**SI Figure 1**). Typically, the first 1–3 layers of Fe_xTaS_2 that interface SiO_2 are deformed and blurred, while up to one layer is blurred at the hBN/ TaS_2 interface. This deformation and apparent amorphization of layers stems from the FIB preparation. We conclude this based on the Raman spectra of atomically thin devices before the FIB process. These Raman spectra retain vibrational modes associated with layer vibrations, which would be absent for amorphous or completely deformed samples (**Figure 4**).

2 CHEMICAL INTERCALATION

Acetone (Sigma-Aldrich) was freeze-pump-thawed and then dried over CaCl_2 (Acros Organics) for more than 12 hours before the reaction. Acetonitrile (Fisher Scientific) and toluene (Fisher Scientific) were obtained from a solvent purification system and dried over 3 Å molecular sieves for at least 12 hours before the reaction. All solvents were handled under an inert atmosphere and passed through a 0.2 μm PTFE syringe membrane filter (VWR) before use to prevent the introduction of particulate matter into the reaction flask.

2.1 Methods for intercalation of zerovalent iron precursors

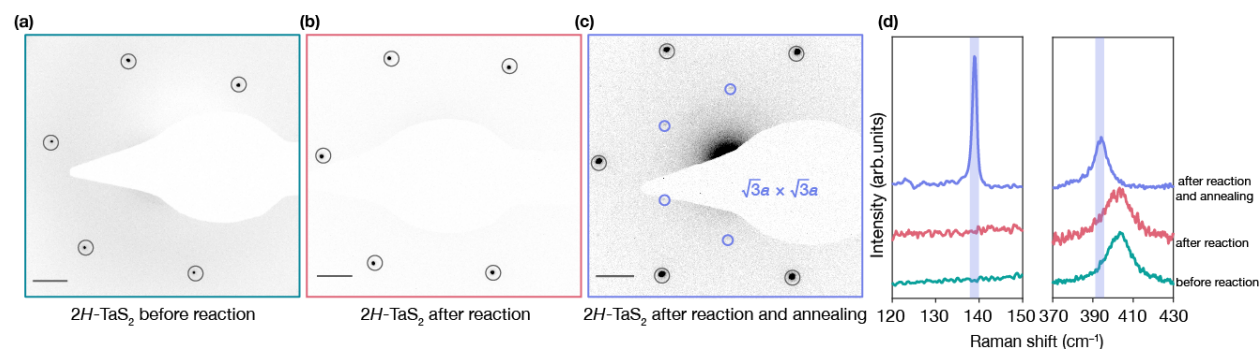
2.1.1 Method 1: Intercalation with $\text{Fe}(\text{CO})_5$ in toluene

10 mL of toluene, a Teflon boat, and a Teflon-coated stir bar were added to a glass scintillation vial and heated to 55 °C in a hotplate heating block. Then, mechanically exfoliated 2H- TaS_2 (HQ Graphene) on a supporting substrate was placed into the Teflon boat and 14 μL of $\text{Fe}(\text{CO})_5$ (Sigma Aldrich) was dispensed into the reaction vial. The vial was closed with a Teflon cap and the solution was left to stir for ~ 24 hours at 55 °C with a dim white light placed next to the vial to promote slow $\text{Fe}(\text{CO})_5$ photodecomposition. After the reaction, the chip was washed three times in warm toluene and then dried in Ar. The sample was then annealed in high-vacuum (approximately 10^{-7} torr) by rapidly warming to 120 °C at 60 °C/min with a 5 minute hold, followed by heating at 11.5 °C/min to 350 °C and a 30 minute hold at 350 °C, before cooling to room temperature at 13.5 °C/min.

2.1.2 Method 2: Intercalation with $\text{Fe}(\text{CO})_5$ in acetonitrile or acetone

In an Ar-filled glovebox, mechanically exfoliated $2H\text{-TaS}_2$ (HQ Graphene) flakes on a supporting substrate were placed into a round-bottom flask and sealed. The flask was evacuated and flushed with N_2 gas on a Schlenk line. Dry, degassed solvent (10 mL) was added to the flask and heated to 50°C . $14\ \mu\text{L}$ (0.02 g) of $\text{Fe}(\text{CO})_5$ was then injected into the reaction flask which was maintained at 50°C for 24 hours under flowing N_2 . During the reaction, a dim white light was placed next to the flaks to promote slow $\text{Fe}(\text{CO})_5$ decomposition. After 24 h, the chip was rinsed three times in dry solvent, followed by another rinse in degassed acetone and ethanol. The sample was then annealed in high-vacuum conditions using the same procedure described in Method 1.

The annealing step was added to the synthetic procedure because Raman modes and NBED diffraction spots associated with Fe ordering emerge only after intercalated samples have been vacuum annealed (SI Figure 5a–d). Furthermore, another indicator of intercalation and charge transfer from Fe to $2H\text{-TaS}_2$ —the red-shift of the A_{1g} peak^{4,5}—occurs only after the annealing procedure (SI Figure 5d). These data suggest that annealing is important in intercalant ordering and charge transfer between intercalated Fe and the $2H\text{-TaS}_2$ lattice.



SI Figure 5. Selected area electron diffraction (SAED) pattern of a $2H\text{-TaS}_2$ flake suspended on a TEM grid (a) before the intercalation, (b) after intercalation and (c) after intercalation and annealing. The first order Bragg spots of the $2H\text{-TaS}_2$ host lattice and the Fe superlattices are marked in the NBED patterns. (d) Raman spectra of a $2H\text{-TaS}_2$ flake on SiO_2/Si : (a) before intercalation, (2) after intercalation and (3) after intercalation and annealing. The Raman spectra are normalized to the A_1/A_{1g} peak. The Raman data was smoothed with the Savitzky–Golay filter.

2.2 Insights into the carbonyl intercalation chemistry

Though a comprehensive mechanistic study of the carbonyl intercalation mechanism is beyond the scope of this work, we use our experimental results and observations to hypothesize plausible intercalation mechanisms.

Previous reports suggest that Fe intercalation into Bi_2Se_3 proceeds via the decomposition of zero-valent $\text{Fe}(\text{CO})_5$.⁶ However, a detailed mechanism of this intercalation remains unclear. Notably, thermally induced

dissociation of $\text{Fe}(\text{CO})_5$ under our reaction conditions (50–55 °C) should be unfavorable based on the documented Fe–CO bond dissociation energies (BDEs) ranging from 17 to 45 kcal/mol.⁷ However, illumination with wavelengths < 635 nm is expected to provide enough energy for Fe–CO photodecomposition.⁷ Congruent with a photodecomposition mechanism, we found that illumination during the reaction is necessary for the success of the intercalation.

To gain additional information about the intercalated Fe species after the reaction and annealing, we cross-sectioned samples using focused ion beam and performed differential phase contrast (DPC) STEM imaging with atomic resolution (**Figure 1c**). We found that the intercalants occupy octahedral interstitial sites in the vdW lattice with no evidence of remaining Fe–CO species.

To gain insight into the ordering of Fe intercalant species, we turn to Raman spectroscopy and NBED diffraction. After the reaction, but before annealing, we do not observe significant changes to the Raman spectra or NBED diffraction patterns of reacted $2H\text{-TaS}_2$ flakes (**SI Figure 5**). However, after post-reaction annealing, the A_{1g} mode of the host lattice typically red-shifts by 5–10 cm^{-1} , which is consistent with electron doping of the $2H\text{-TaS}_2$ lattice (**SI Figure 5**).^{4,5} Additionally, annealed flakes exhibit low frequency Raman modes (130–140 cm^{-1}) and NBED diffraction spots, both signifying structural iron ordering (**SI Figure 5**).⁸ Based on these results, we speculate that prior to annealing, the intercalants are structurally disordered and may remain in a zero-valent state (or a nearly zero-valent state). On the other hand, after annealing, the Fe intercalants electron-dope the $2H\text{-TaS}_2$ lattice and order within the vdW gap, consistent with bulk Fe_xTaS_2 .

2.3 Nanofabrication

All nanofabrication steps were performed in the Marvell Nanofabrication Laboratory after the chemical intercalation and annealing of samples. In a typical fabrication procedure, we used electron beam lithography (Crestec CABL-UH Series Electron Beam Lithography System) to define electrical contacts. Reactive ion etching (RIE) with a mixture of 35 sccm CHF_3 and 5 sccm O_2 (Plasma-Therm PK-12 RIE) for 30 seconds was used to remove hBN and expose fresh Fe_xTaS_2 . Immediately afterwards, Cr/Pt (2 nm/100 nm) was evaporated onto Fe_xTaS_2 (NRC thermal evaporator).

After lift-off, electron-beam lithography was used to define a Hall bar-shaped etch mask. The subsequent etching of the Hall bar shape for thin samples (< 6 layers) was performed by reactive ion etching with 35 sccm CHF_3 and 5 sccm O_2 . On the other hand, thicker samples were etched with ~25 etch cycles of XeF_2 (Xetch instrument) for 20 seconds at 3.2 Torr. After the hBN/ Fe_xTaS_2 etching, the samples were cleaned for 20 seconds in a 40 sccm O_2 plasma and subsequently the residual PMMA resist was dissolved in acetone.

3 ELECTRON MICROSCOPY AND RAMAN SPECTROSCOPY

3.1 Transmission electron microscopy (TEM)

High-resolution TEM and nanobeam electron diffraction (NBED) measurements were performed on a JEOL 2100-F TEM operated at 200 kV at the Molecular Foundry. For NBED, the nanobeam spot radius was set to 90 nm. Selected area electron diffraction (SAED) patterns were obtained with a 40 μm diameter aperture using an FEI Tecnai T20 S-TWIN TEM operated at 200 kV.

STEM-EDS of cross-sectional TEM samples was performed on the FEI TitanX microscope at the National Center for Electron Microscopy (NCEM). The microscope was operated at 60 kV with a probe convergence angle of 10 mrad and a beam current of ~ 150 pA. The total acquisition time varied from 3 to 20 minutes, depending on the signal-to-noise ratio. STEM-EDS maps were collected in multiple regions of the cross-sectional samples, and the averages and standard deviations of these data sets were reported in the main paper.

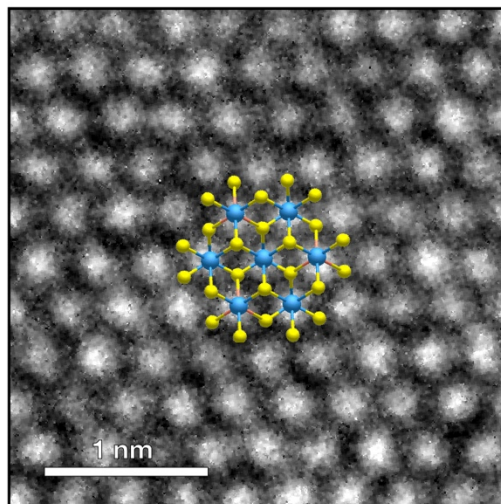
HRSTEM imaging of layers was conducted on an FEI TitanX microscope operated at 200 kV with a convergence angle of 10 mrad and a half collection angle of 52 mrad.

Differential phase contrast (DPC) STEM measurements were acquired on the TEAM 0.5, which is a Titan 80-300 with a probe corrector, at NCEM. The microscope's accelerating voltage was 300 kV, the convergence angle was 30 mrad, and the beam current was 70 pA. The 4D-STEM scans were acquired using the 4D Camera with a frame time of 11 μsec per probe position, 576×576 pixels, and 1024×1024 probe positions. The DPC-STEM data was acquired simultaneously with HAADF-STEM images.

Electron energy loss spectroscopy measurements were acquired on the TEAM 1 which is a Titan 80-300 with a probe corrector. The microscope's accelerating voltage was 300 kV, the convergence angle was 17.1 mrad, and the beam current was 87 pA. The collection semi angle was 41.9 mrad. The dispersion on the spectrometer was 90 meV/channel. Spectra was summed over three passes across the samples, with an exposure of 0.01 seconds/pixel.

3.2 Results of high-resolution TEM (HRTEM) imaging

High-resolution TEM imaging of Fe_xTaS_2 crystals along the c -axis revealed that the ab atomic periodicities match the expected values for bulk Fe_xTaS_2 (SI Figure 6).⁹



SI Figure 6. HRTEM of a Fe_xTaS₂ crystal imaged along the *c*-axis of the flake. A CIF file of Fe_{1/3}TaS₂ (ref 9) along the [0001] axis is overlaid with the micrograph.

3.3 STEM-EDS analysis

Analysis of the STEM-EDS data was carried out in the Bruker Esprit 1.9 software. Series Fit deconvolution was employed to deconvolute overlapping peaks. Next, to estimate the atomic percentage (at. %) of the amount of Fe coming from the TEM column, we analyzed a 2H-TaS₂ sample that was not intercalated. We determined that the at. % ratio of Fe to Co coming from the column is approximately 1:1. Thus, by identifying the at. % of Co in the EDS signal of our intercalated samples, it was possible to determine the amount of signal coming from the stainless-steel column. This “column iron” background contribution was subtracted from the total Fe at. % to determine the final iron intercalation amount.

To compare the Fe:Ta stoichiometry measured in thin flakes with the values determined for bulk (3D) crystals, we consider that terminating Ta ions (in the top and bottom TaS₂ layers) significantly contribute to the measured elemental composition of thin crystals. So, the continuous periodicity along the *c*-axis, characteristic for bulk Fe_xTaS₂ crystals, is not present in thin flakes. Consequently, the unit cell differs for structurally equivalent crystals with different number of layers (**SI Figure 7**). As a result of this, the Fe/Ta ratio is lower in thin samples compared to their structurally equivalent 3D analogues. This is demonstrated in SI Figure 7, where crystals with varying thickness and equivalent $\sqrt{3}a \times \sqrt{3}a$ iron superstructure are shown. The Fe/Ta ratio of thin flakes with *L* number of layers can be related to the bulk Fe/Ta ratio (1/3) using the following equation:

$$x_{thin}(L) = 0.33 - 0.33/L \quad (1)$$

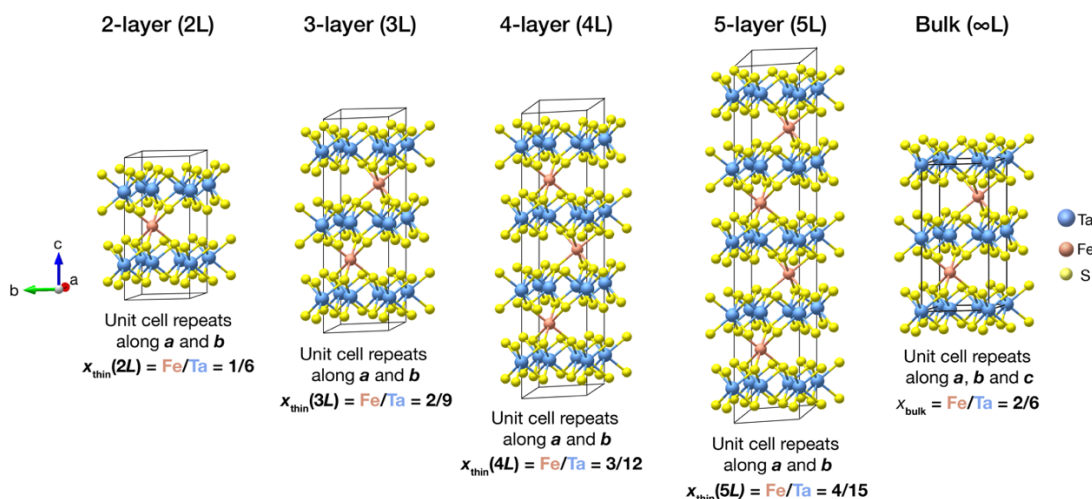
Equation (1) can be generalized to:

$$x_{thin}(L) = x_{bulk} - x_{bulk}/L \quad (2)$$

By rearranging Equation (2), we obtain:

$$x_{bulk} = x_t / \left(1 - \frac{1}{L}\right) \quad (3)$$

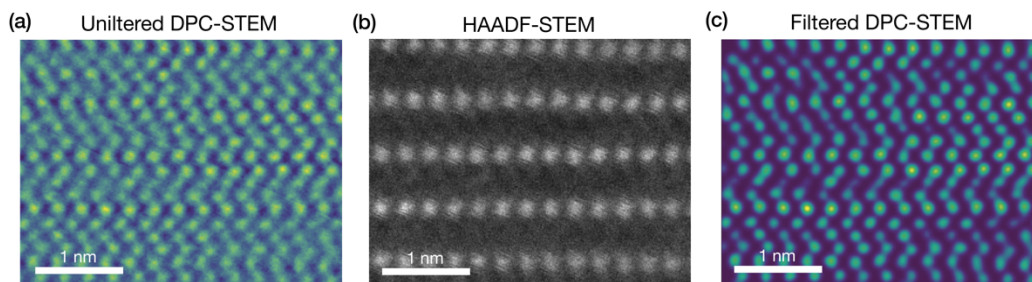
Equation 3 can be used to convert between the Fe:Ta values measured in thin samples (x_{thin} or x_t) possessing L number of layers and the stoichiometry of their compositionally equivalent bulk analogues (x_{bulk} or x_b).



SI Figure 7. Unit cell of structurally equivalent crystals with different number of layers. The displayed crystals exhibit the $\sqrt{3}a \times \sqrt{3}a$ iron superstructure.

3.4 Filtering of DPC-STEM micrographs

Raw DPC images (**SI Figure 8a**), which are acquired simultaneously with HAADF-STEM images (**SI Figure 8b**), were filtered via thresholding. The threshold was calculated using Otsu's method. The mask from thresholding is further refined using morphological opening with a disk-shaped structuring element that has a radius of 2 pixels. This final mask is then multiplied by an FFT filtered version of the raw data. The resulting image is finally convolved with a 2D gaussian to yield the final filtered image (**SI Figure 8c**).

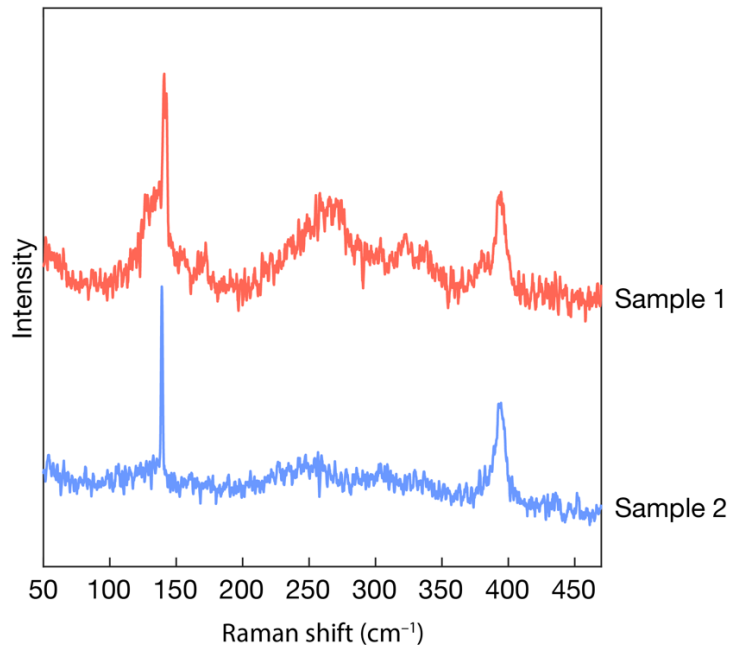


SI Figure 8. (a) Representative raw DCP-STEM image of a cross-sectional Fe_xTaS_2 sample. (b) HAADF-STEM image acquired in the identical sample region as (a). (c) Filtered version of the DPC-STEM image (a).

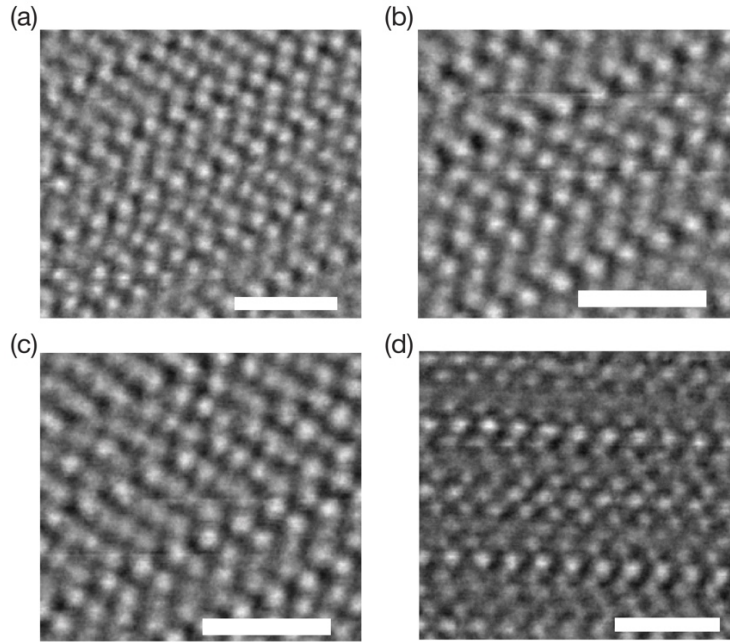
3.5 Analysis of the Fe trigonal distortion from DPC-STEM data

To investigate the coordination environment of intercalated Fe, we analyzed DPC-STEM micrographs of four regions across two Fe_xTaS_2 samples (368 inter-sulfur distances). Both measured samples exhibited prominent Raman modes corresponding to the $\sqrt{3}a \times \sqrt{3}a$ iron superstructure (**SI Figure 9**). Cross-sections of these samples were imaged along the $[10\bar{1}0]$ zone axis of the 2H-TaS₂ lattice, with representative DPC-STEM images shown in **Figure 1c** and **SI Figures 8** and **10**.

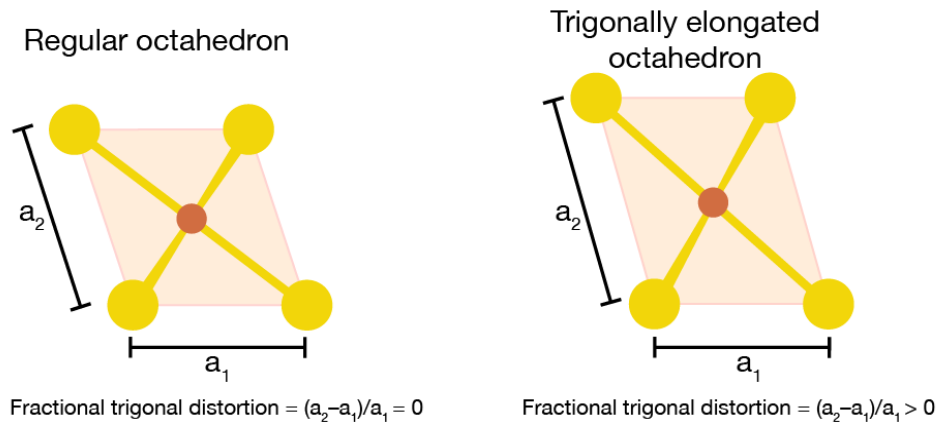
We determined the location of all atoms using local peak finding after convolving with a 2D gaussian. Then, we assigned element labels to each location by first matching Ta locations in the simultaneously acquired HAADF image (**SI Figure 8b**), and then labeling the S and Fe site based on distance from Ta sites. The location of the Fe and S sites were then refined by iteratively fitting each Fe and S site to a gaussian. The method is instantiated with the locations from the local peak finding. We then refine the location and gaussian using least squares fitting. Following this procedure, each refined Fe site was matched to its four coordinated sulfur sites to measure the trigonal distortions, as defined in **SI Figure 11**. A trigonal distortion of 8.0(6) % was as found after measuring 368 inter-sulfur distances. Note that we report the standard error as the uncertainty of the trigonal distortion.



SI Figure 9: The Raman spectra of Fe_xTaS_2 that were cross-sectioned and measured with DPC-STEM. The Raman spectra are normalized to the A_1/A_{1g} peak. The data was smoothed with the Savitzky–Golay filter.



SI Figure 10: Unfiltered DPC-STEM micrographs for (a)-(c) Fe_xTaS_2 sample 1 and (d) Fe_xTaS_2 sample 2. Scale bars: 1 nm.

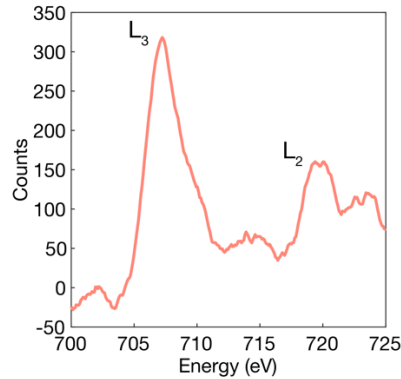


SI Figure 11. Schematic of perfect octahedral (left) and trigonally distorted (right) octahedral Fe environments, as seen along the $[10\bar{1}0]$ zone axis of the $2H\text{-TaS}_2$ lattice. The fractional trigonal distortion is defined as $(a_2 - a_1)/a_1$. The distortion is: (1) zero for a regular octahedron and (2) greater than zero for the trigonally elongated Fe environment.

3.6 Analysis and results of electron energy loss spectroscopy (EELS)

To isolate the EELS signal from the background, a power law background subtraction was performed using the Gatan DigitalMicrograph Software. We evaluated the integrated L_3/L_2 edge area ratio with step function

subtraction. For the measured data (SI Figure 12), the L_3/L_2 ratio was 3.9(3), while the energy of the L_3 edge was 707 eV. These data are consistent with a +2 oxidation state of iron.¹⁰



SI Figure 12. Background-subtracted EELS spectrum of Fe acquired for a cross-sectional Fe_xTaS_2 sample. The data have been smoothed with the Savitzky–Golay filter.

3.7 Raman spectroscopy

Ultra-low frequency (ULF) Raman spectroscopy (Horiba Multiline LabRam Evolution) was conducted using a 633 nm laser excitation at a power of 50–80 μW with 10 second acquisition times and five accumulations. Baseline correction was performed by fitting a polynomial curve to the background. Raman maps of the Hall bar channel were obtained after magnetotransport measurements, with typical step sizes of 1 μm . These spectra were summed to obtain cumulative Raman spectra displayed in the main paper.

4 MAGNETOTRANSPORT MEASUREMENTS

Transport measurements were performed using standard lock-in techniques. In brief, a small 0.5–1 μA alternating current (17.777 Hz) was applied between the source and drain contacts. Concurrently, the four-probe longitudinal (V_{xx}) and transverse (V_{xy}) voltage drops were measured with a lock-in amplifier (Stanford Research SR830). All phases were $\leq 3^\circ$ and so from the measured values, resistances could be determined with Ohm's law. Measurements were obtained across the Hall bar channel, and values extracted from these measurements (e.g. coercive fields) were averaged from all measured values. The standard deviation (1σ) obtained from these measurements is reported as the error in the main paper.

4.1 Symmetrization of magnetotransport data

To eliminate the mixing of R_{xx} and R_{xy} signals, we symmetrized (anti-symmetrized) our data with the established approach:¹¹

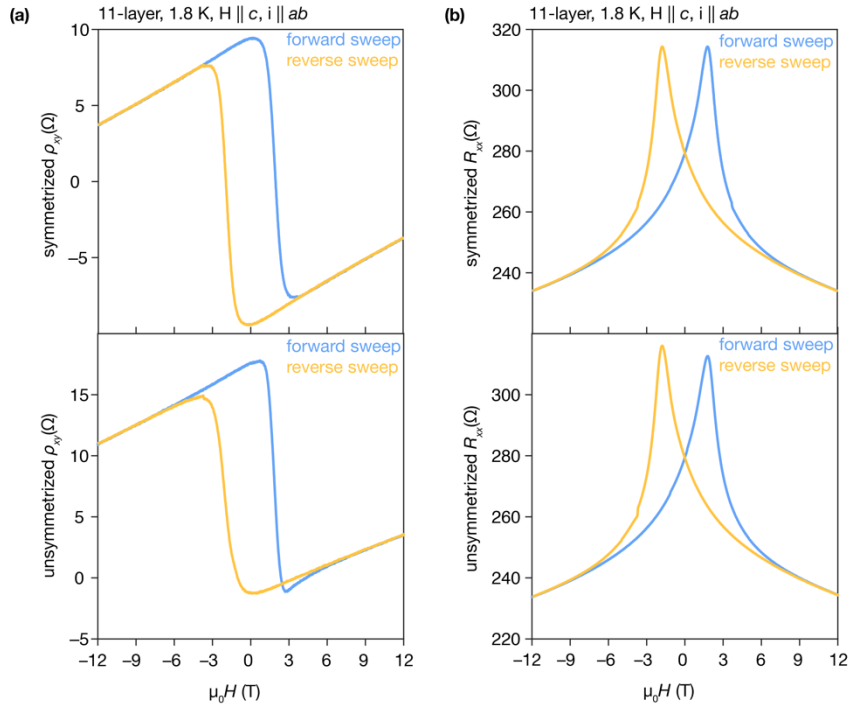
$$R_{xx,symm}^{Forward}(\mu_0 H) = \frac{1}{2} [R_{xx,raw}^{Forward}(\mu_0 H) + R_{xx,raw}^{Reverse}(-\mu_0 H)]$$

$$R_{xx,symm}^{Reverse}(\mu_0 H) = \frac{1}{2} [R_{xx,raw}^{Reverse}(\mu_0 H) + R_{xx,raw}^{Forward}(-\mu_0 H)]$$

$$R_{xy,symm}^{Forward}(\mu_0 H) = \frac{1}{2} [R_{xy,raw}^{Forward}(\mu_0 H) - R_{xy,raw}^{Reverse}(-\mu_0 H)]$$

$$R_{xy,symm}^{Reverse}(\mu_0 H) = \frac{1}{2} [R_{xy,raw}^{Reverse}(\mu_0 H) - R_{xy,raw}^{Forward}(-\mu_0 H)]$$

Our raw magnetotransport data are hysteretic before and after the symmetrization (anti-symmetrization) procedure (SI Figure 13), confirming that the observed hysteresis are not an artefact of the data processing.



SI Figure 13. Symmetrized and unsymmetrized (a) ρ_{xy} and (b) R_{xx} for a the 11-layer Fe_xTaS_2 device.

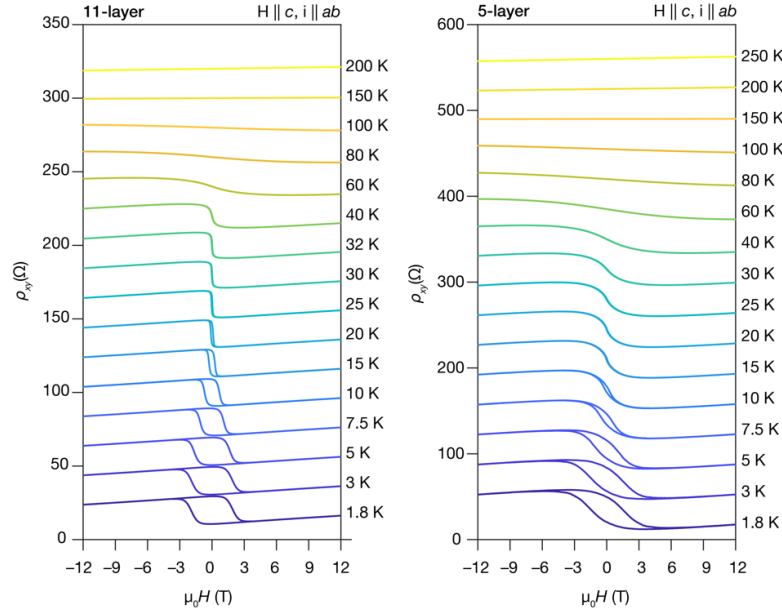
4.2 Analysis of the ordinary Hall effect (OHE)

The symmetrized transverse (Hall) resistivity (ρ_{xy}) was used to extract the sample's carrier type and density. To accomplish this, the ordinary Hall effect (OHE) term is fitted to the equation:

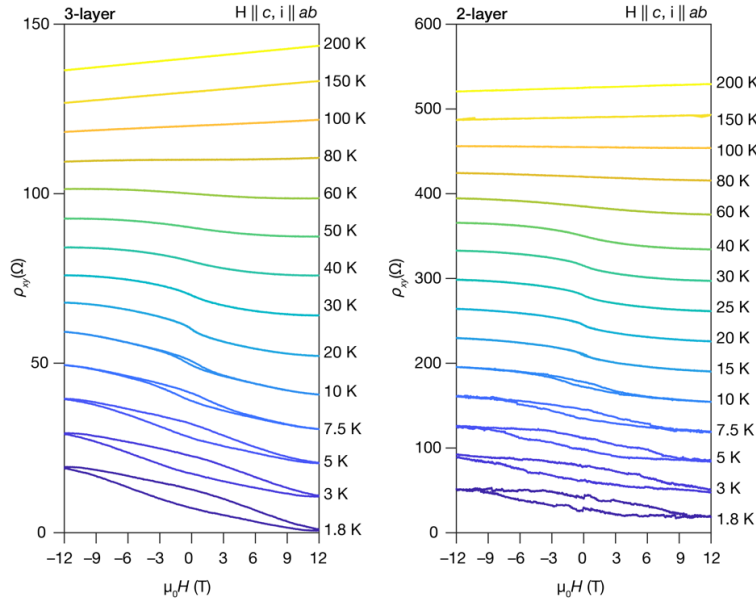
$$\rho_{OHE} = \frac{1}{ne} \mu_0 H$$

where n is the carrier density, e is the elementary charge, μ_0 is the vacuum permeability, and H is the applied field. The fitting is performed on the linear ρ_{xy} signal where ρ_{OHE} is dominant. For all samples, the OHE term is dominant at all magnetic fields well above their T_C . For the 5-layer and 11-layer samples, the OHE term is

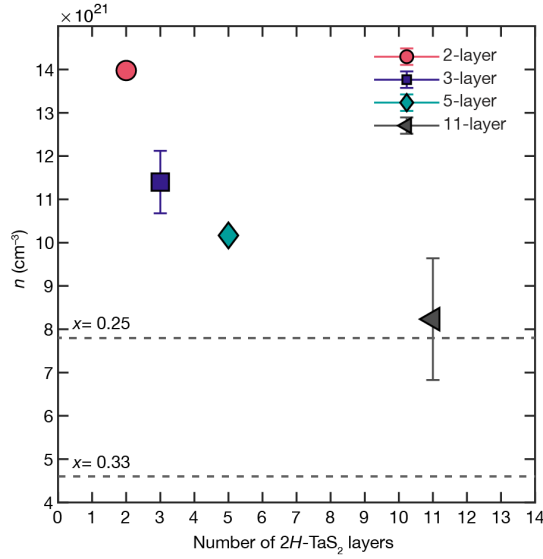
also dominant at high magnetic fields below their magnetic ordering temperatures (**SI Figure 14**). In contrast, for the 2-layer and 3-layer samples, the ρ_{xy} signal is nonlinear below the T_C irrespective of the applied magnetic field. This points to the strong presence of the anomalous Hall effect at low temperatures in the entirety of the measured field range (**SI Figure 15**). Thus, for the 2-layer and 3-layer samples, we determined n well above the T_C , where the OHE term is dominant at all applied magnetic fields. As follows, to compare the carrier densities of different devices, we plot their n at 200 K (**SI Figure 16**), where OHE term can be analyzed for all devices.



SI Figure 14. Symmetrized ρ_{xy} for the 11-layer $\text{Fe}_{0.29(2)}\text{TaS}_2$ and 5-layer $\text{Fe}_{0.38(4)}\text{TaS}_2$ devices.



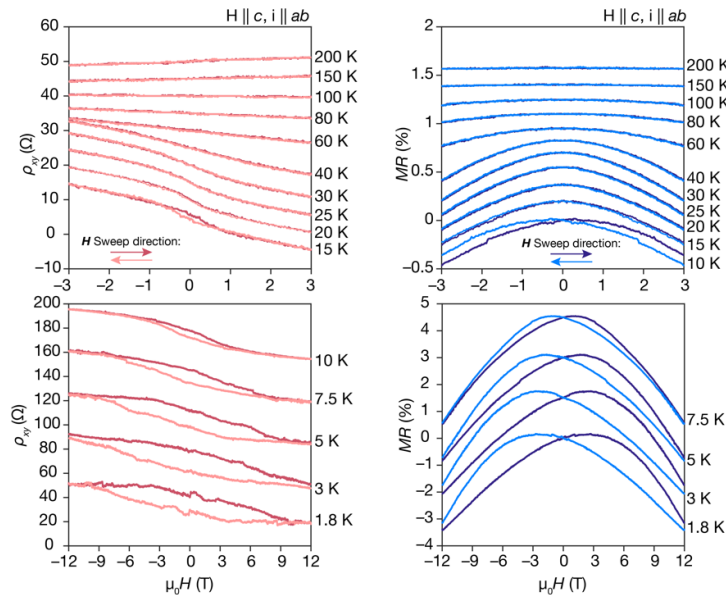
SI Figure 15. Symmetrized ρ_{xy} for the 3-layer $\text{Fe}_{0.37(2)}\text{TaS}_2$ and 2-layer $\text{Fe}_{0.58(14)}\text{TaS}_2$ devices.



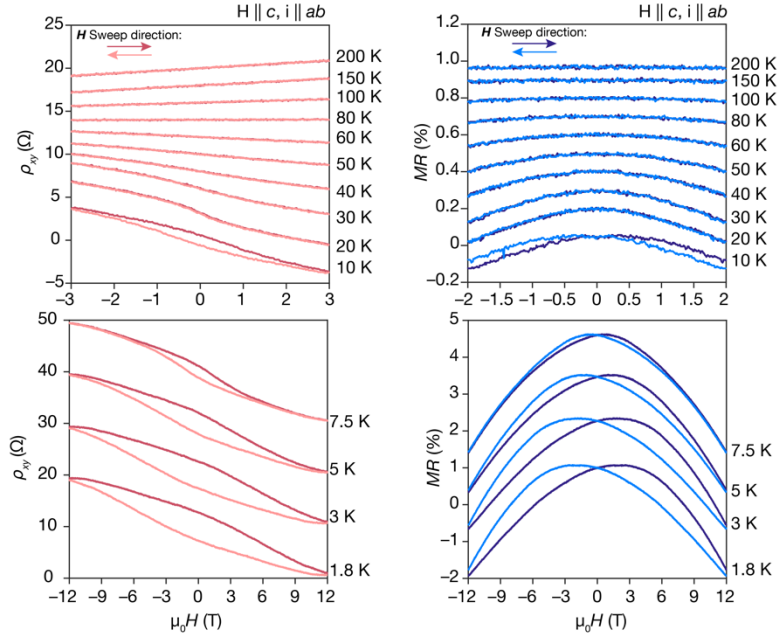
SI Figure 16. Carrier density of measured Fe_xTaS_2 devices obtained from fitting the ordinary Hall effect term (ρ_{OHE}) at 200 K. Carrier density values for bulk $x = 0.25$ ¹² and $x = 0.33$ ¹³ crystals, which were extracted from the literature, are indicated in dashed lines.

4.3 Temperature dependence of hysteretic behavior in 2-, 3-, and 5- layer crystals

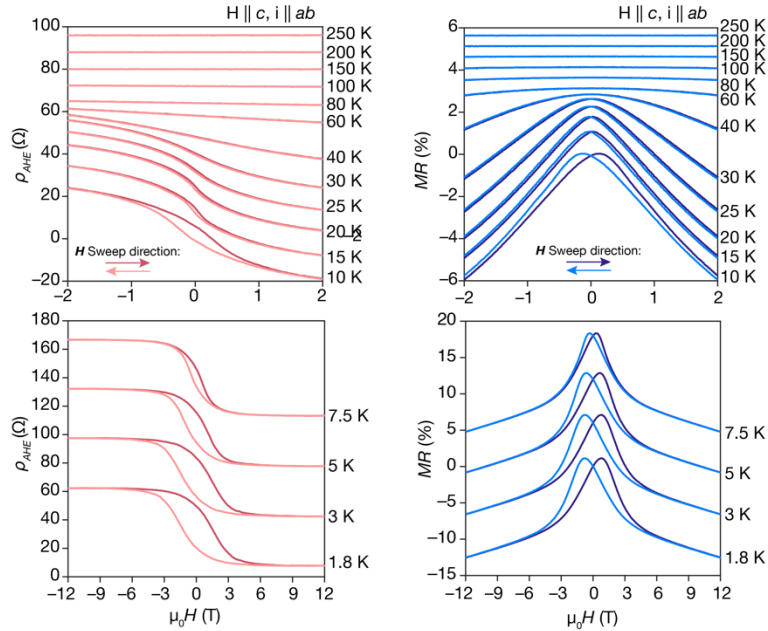
We examined the temperature range at which the 2-, 3-, and 5- layer Fe_xTaS_2 devices evince hysteretic features in ρ_{xy} (or ρ_{AHE}) and magnetoresistance (MR) (SI Figure 17–19). The bilayer’s ρ_{xy} and MR hystereses close between 20 to 25 K (SI Figure 17). On the other hand, for the 3-layer and 5-layer samples, the hysteretic features vanish between 10–20 K (SI Figure 18) and 40–60 K (SI Figure 19), respectively.



SI Figure 17. Temperature dependence of the symmetrized ρ_{xy} and magnetoresistance (MR) for the bilayer $\text{Fe}_{0.58(14)}\text{TaS}_2$ device.



SI Figure 18. Temperature dependence of the symmetrized ρ_{xy} and magnetoresistance (MR) for the 3-layer $\text{Fe}_{0.37(2)}\text{TaS}_2$ device.



SI Figure 19. Temperature dependence of the symmetrized anomalous Hall resistivity (ρ_{AHE}) and magnetoresistance (MR) for the 5-layer $\text{Fe}_{0.38(4)}\text{TaS}_2$ device.

For the 5-layer sample, we were able to fit the OHE term at temperatures above and below the T_C (SI Section 4.2), enabling us to separate it from the ρ_{AHE} term in the full measured temperature range (SI Figure 19). This allowed us to extract the remanent ρ_{AHE} at $H = 0$ for the 5-layer sample. Unlike in materials with a single

magnetic phase transition¹⁴, we did not observe a singular inflection in the ρ_{AHE} versus T (SI Figure 20), indicating that this sample may exhibit multiple magnetic phase transitions.

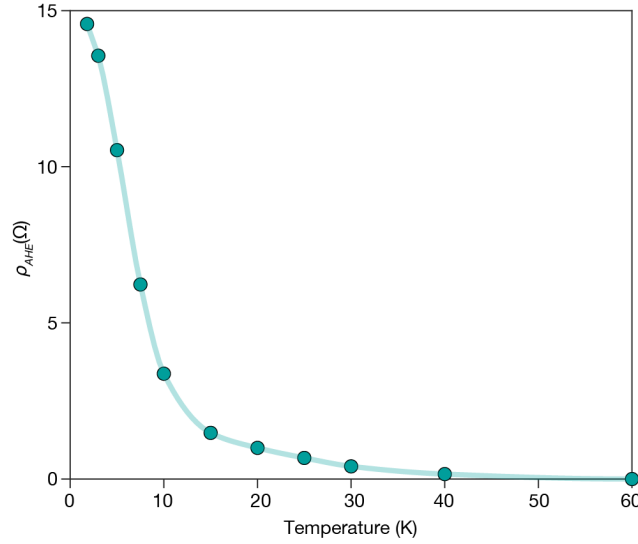
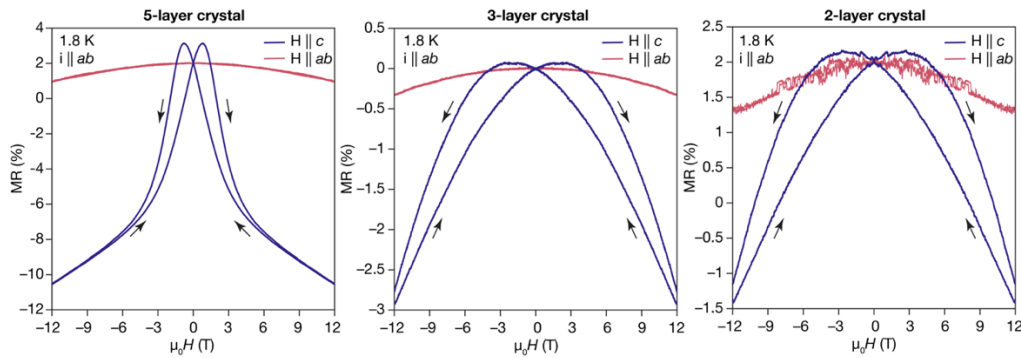


Figure 20. Temperature dependence of the remanent ρ_{AHE} for the 5-layer $\text{Fe}_{0.38(4)}\text{TaS}_2$ device.

4.4 Magnetoresistance of the 5-, 3- and 2-layer crystals with $H||c$ and $H||ab$

To experimentally probe the magnetocrystalline anisotropy (MCA) of the 2-, 3- and 5-layer crystals, we measured their magnetoresistance while sweeping the external magnetic field parallel and perpendicular to the c -axis of the crystals (SI Figure 21). Hysteresis in MR is only seen when the field is parallel to the c -axis ($H||c$), which confirms the large out-of-plane MCA in the thin crystals.



SI Figure 21. MR of the 5-layer $\text{Fe}_{0.38(4)}\text{TaS}_2$, 3-layer $\text{Fe}_{0.37(2)}\text{TaS}_2$ and 2-layer $\text{Fe}_{0.58(14)}\text{TaS}_2$ crystals with the external magnetic field parallel and perpendicular to the crystallographic c -axis.

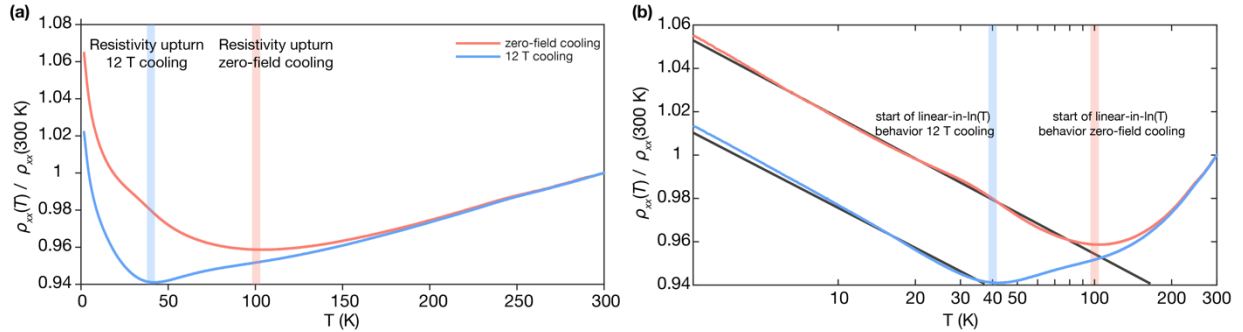
4.5 Criticality fits

The Curie temperature and the critical exponent (β) for our materials can be extracted from the temperature dependence of the remanent ρ_{AHE} signal. Using the method of least squares, we fit the remanent

ρ_{AHE} to the critical power-law form: $\alpha(1-T/T_C)^\beta$, with α, β and T_C as simultaneous fitting parameters.¹⁴ We found the obtained β value changes by varying the temperature fitting interval. However, irrespective of the temperature fitting interval around T_C , all obtained values were within 0.03 of one another and congruent with the Ising model.

4.6 Origin of the resistivity upturn for bilayer Fe_xTaS_2

For the bilayer device, the resistivity exhibits an upturn at low temperatures, reaching a value higher than the room temperature resistivity. The onset temperature of this upturn (T^*) is dependent on the magnetic field applied upon cooling the sample (SI Figure 22a). When the sample is cooled in zero magnetic field, the resistivity upturn occurs at ~ 98 K. On the other hand, when a 12 T out-of-plane field is applied, T^* shifts to a lower temperature of ~ 42 K. Below T^* , the resistivity is linear in $\ln(T)$ (SI Figure 22b). This $\ln(T)$ dependence indicates that the possible reasons for the observed behavior are electron–electron interactions, weak localization (WL), or the Kondo effect.^{15–17} We can exclude electron–electron interactions from the possible contributors to the observed behavior, because T^* is suppressed by the applied field.^{18–21} Thus, the observed resistivity upturn occurs due to WL and/or the Kondo effect. However, additional studies that are outside the scope of this study will be needed to separate the contributions from these two phenomena.

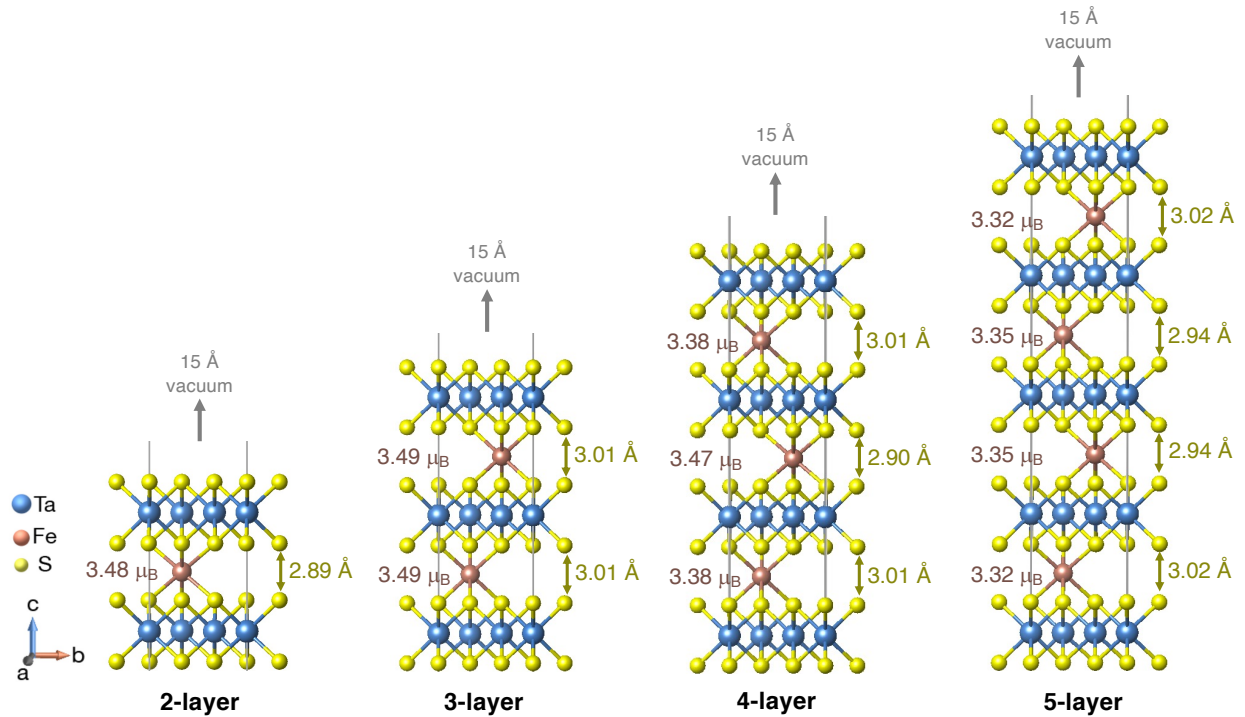


SI Figure 22. (a) Temperature-dependent resistivity of the bilayer $\text{Fe}_{0.58(14)}\text{TaS}_2$ device upon cooling in zero magnetic field (blue line) and a 12 T ($H \parallel c$) magnetic field (orange line). (b) Data from (a) with the temperature plotted on the natural log scale. Black lines are linear fits to the data below the resistivity upturn temperature.

5 DETAILS OF THE THEORETICAL CALCULATIONS

Electronic band structures and density of states were calculated in the density functional theory framework using the Vienna *Ab-initio* Simulation Package (VASP).^{22–25} Projector augmented wave pseudopotentials^{26,27} included Fe $3d^64s^2$, Ta $5p^65d^66s^2$, S $3s^23p^4$ electrons as valence. The structures were constructed in a $\sqrt{3}a \times \sqrt{3}a$ supercell of $2H\text{-TaS}_2$ and a 15 Å vacuum gap was included out-of-plane. The PBEsol exchange–correlation functional²⁸

was used with 800 eV plane wave energy cut-off and a $10 \times 10 \times 1$ Gamma-centered k -point grid, which converged the total energy within 1 meV per formula unit. Hubbard U corrections were applied to the Fe d -orbitals by the Liechtenstein method²⁹ with $U = 4.0$ eV and $J = 0.7$ eV. This is consistent with previous studies that used similar values of U and J to account for the Fe- d localization³⁰. We further validated this choice of U by comparing our calculated lattice parameters of bulk $\text{Fe}_{1/4}\text{TaS}_2$ with experiments, finding that a U of 4.0 eV gave in-plane and out-of-plane lattice parameters within 1% of those measured. Structure optimizations to a force tolerance of $2 \text{ meV}\text{\AA}^{-1}$ gave the following in-plane lattice parameters: 2-layers: 5.723 \AA , 3-layers: 5.729 \AA , 4-layers: 5.718 \AA , and 5-layers: 5.710 \AA . Spin-orbit coupling was included for the magnetocrystalline anisotropy calculations only.



SI Figure 23. Calculated structures and magnetism of $\sqrt{3}a \times \sqrt{3}a$ superlattices of Fe_xTaS_2 for 2-, 3-, 4-, and 5-layers of TaS_2 . The final magnetic moment on each Fe atom (projected in the PAW sphere) is given, in addition to the interlayer separation of the optimized structure.

6 DATA PROCESSING AND PRESENTATION

The denoised Raman data was treated using an empirical Bayesian method with a Cauchy prior (wdenoise function in the Matlab wavelet toolbox) unless indicated otherwise. The crystal structures were visualized with VESTA version 3.5.7 software,³¹ while schematics were drawn in Autodesk 3ds Max and Adobe Illustrator version 26.0.2.

7. REFERENCES

- (1) Li, H.; Wu, J.; Huang, X.; Lu, G.; Yang, J.; Lu, X.; Xiong, Q.; Zhang, H. Rapid and Reliable Thickness Identification of Two-Dimensional Nanosheets Using Optical Microscopy. *ACS Nano* **2013**, *7*, 10344–10353.
- (2) Frisenda, R.; Navarro-Moratalla, E.; Gant, P.; Pérez De Lara, D.; Jarillo-Herrero, P.; Gorbachev, R. V.; Castellanos-Gomez, A. Recent Progress in the Assembly of Nanodevices and van Der Waals Heterostructures by Deterministic Placement of 2D Materials. *Chem. Soc. Rev.* **2018**, *47*, 53–68.
- (3) Cao, Y.; Luo, J. Y.; Fatemi, V.; Fang, S.; Sanchez-Yamagishi, J. D.; Watanabe, K.; Taniguchi, T.; Kaxiras, E.; Jarillo-Herrero, P. Superlattice-Induced Insulating States and Valley-Protected Orbits in Twisted Bilayer Graphene. *Phys. Rev. Lett.* **2016**, *117*, 116804.
- (4) Valencia-Ibáñez, S.; Jimenez-Guerrero, D.; Salcedo-Pimienta, J. D.; Vega-Bustos, K.; Cárdenas-Chirivi, G.; López-Manrique, L.; Galvis, J. A.; Hernandez, Y.; Giraldo-Gallo, P. Raman Spectroscopy of Few-Layers TaS₂ and Mo-Doped TaS₂ with Enhanced Superconductivity. 2022-01-24. arXiv. <https://doi.org/10.48550/ARXIV.2201.09840>. (accessed 2022-02-01).
- (5) Su, T.; Huang, J.; Wang, Q.; Zhang, X.; Zhou, L.; Tang, M.; Zhang, C.; Yuan, H.; Zhao, W.; Wang, Z.; Yuan, H.; Wang, X. Investigation of Phonon Modes in 2H-TaX₂ (X = S/Se) Flakes with Electrostatic Doping. *J. Appl. Phys.* **2021**, *130*, 105302.
- (6) Koski, K. J.; Wessells, C. D.; Reed, B. W.; Cha, J. J.; Kong, D.; Cui, Y. Chemical Intercalation of Zerovalent Metals into 2D Layered Bi₂Se₃ Nanoribbons. *J. Am. Chem. Soc.* **2012**, *134*, 13773–13779.
- (7) González-Blanco, O.; Branchadell, V. Density Functional Study of the Fe–CO Bond Dissociation Energies of Fe(CO)₅. *J. Chem. Phys.* **1998**, *110*, 778–783.
- (8) Fan, S.; Neal, S.; Won, C.; Kim, J.; Sapkota, D.; Huang, F.; Yang, J.; Mandrus, D. G.; Cheong, S.-W.; Haraldsen, J. T.; Musfeldt, J. L. Excitations of Intercalated Metal Monolayers in Transition Metal Dichalcogenides. *Nano Lett.* **2021**, *21*, 99–106.
- (9) Wijngaard, J. H.; Hass, C.; Devillers, M. A. C. Optical and Magneto-Optical Properties of Fe_{0.28}TaS₂. *J. Phys. Condens. Matter.* **1991**, *3*, 6913–6923.
- (10) Tan, H.; Verbeeck, J.; Abakumov, A. M.; van Tendeloo, G. Oxidation State and Chemical Shift Investigation in Transition Metal Oxides by EELS. *Ultramicroscopy* **2012**, *116*, 24–33.
- (11) Gao, A.; Liu, Y.-F.; Hu, C.; Qiu, J.-X.; Tzschaschel, C.; Ghosh, B.; Ho, S.-C.; Bérubé, D.; Chen, R.; Sun, H.; et al. Layer Hall Effect in a 2D Topological Axion Antiferromagnet. *Nature* **2021**, *595*, 521–525.

- (12) Checkelsky, J. G.; Lee, M.; Morosan, E.; Cava, R. J.; Ong, N. P. Anomalous Hall Effect and Magnetoresistance in the Layered Ferromagnet $\text{Fe}_{1/4}\text{TaS}_2$: The Inelastic Regime. *Phys. Rev. B* **2008**, *77*, 14433.
- (13) Mangelsen, S.; Hansen, J.; Adler, P.; Schnelle, W.; Bensch, W.; Mankovsky, S.; Polesya, S.; Ebert, H. Large Anomalous Hall Effect and Slow Relaxation of the Magnetization in $\text{Fe}_{1/3}\text{TaS}_2$. *J. Phys. Chem. C* **2020**, *124*, 24984–24994.
- (14) Fei, Z.; Huang, B.; Malinowski, P.; Wang, W.; Song, T.; Sanchez, J.; Yao, W.; Xiao, D.; Zhu, X.; May, A. F.; Wu, W.; Cobden, D. H.; Chu, J.-H.; Xu, X. Two-Dimensional Itinerant Ferromagnetism in Atomically Thin Fe_3GeTe_2 . *Nat. Mater.* **2018**, *17*, 778–782.
- (15) Liu, H.; Bao, L.; Zhou, Z.; Che, B.; Zhang, R.; Bian, C.; Ma, R.; Wu, L.; Yang, H.; Li, J.; et al. Quasi-2D Transport and Weak Antilocalization Effect in Few-Layered VSe_2 . *Nano Lett.* **2019**, *19*, 4551–4559.
- (16) Jobst, J.; Kisslinger, F.; Weber, H. B. Detection of the Kondo Effect in the Resistivity of Graphene: Artifacts and Strategies. *Phys. Rev. B - Condens. Matter Mater. Phys.* **2013**, *88*, 1–6.
- (17) Cao, Q.; Yun, F. F.; Sang, L.; Xiang, F.; Liu, G.; Wang, X. Defect Introduced Paramagnetism and Weak Localization in Two-Dimensional Metal VSe_2 . *Nanotechnology* **2017**, *28*, 475703.
- (18) Wang, Y.; Xie, C.; Li, J.; Du, Z.; Cao, L.; Han, Y.; Zu, L.; Zhang, H.; Zhu, H.; Zhang, X.; et al. Weak Kondo Effect in the Monocrystalline Transition Metal Dichalcogenide ZrTe_2 . *Phys. Rev. B* **2021**, *103*, 1–8.
- (19) Liu, H.; Xue, Y.; Shi, J. A.; Guzman, R. A.; Zhang, P.; Zhou, Z.; He, Y.; Bian, C.; Wu, L.; Ma, R.; et al. Observation of the Kondo Effect in Multilayer Single-Crystalline VTe_2 Nanoplates. *Nano Lett.* **2019**, *19*, 8572–8580.
- (20) Li, Y.; Deng, R.; Lin, W.; Tian, Y.; Peng, H.; Yi, J.; Yao, B.; Wu, T. Electrostatic Tuning of Kondo Effect in a Rare-Earth-Doped Wide-Band-Gap Oxide. *Phys. Rev. B* **2013**, *87*, 155151.
- (21) Hien-Hoang, V.; Chung, N.-K.; Kim, H.-J. Electrical Transport Properties and Kondo Effect in $\text{La}_{1-x}\text{Pr}_x\text{NiO}_{3-\delta}$ thin Films. *Sci. Rep.* **2021**, *11*, 5391.
- (22) Kresse, G. & Hafner, J. Ab initio molecular dynamics for liquid metals. *Physical Review B* **1993**, *47*, 558-561.
- (23) Kresse, G. & Hafner, J. Ab initio molecular-dynamics simulation of the liquid-metal-amorphous-semiconductor transition in germanium. *Physical Review B* **1994**, *49*, 14251-14269.
- (24) Kresse, G. & Furthmüller, J. Efficient iterative schemes for ab initio total-energy calculations using a plane-wave basis set. *Physical Review B* **1996**, *54*, 11169-11186.

- (25) Kresse, G. & Furthmüller, J. Efficiency of ab-initio total energy calculations for metals and semiconductors using a plane-wave basis set. *Computational Materials Science* **1996**, 6, 15-50.
- (26) Blöchl, P. E. Projector augmented-wave method. *Physical Review B* **1994**, 50, 17953-17979.
- (27) Kresse, G. & Joubert, D. From ultrasoft pseudopotentials to the projector augmented-wave method. *Physical Review B* **1999**, 59, 1758-1775.
- (28) Csonka, G.I., Perdew, J.P., Ruzsinszky, A., Philipsen, P.H., Lebègue, S., Paier, J., Vydrov, O.A. and Ángyán, J.G. Assessing the performance of recent density functionals for bulk solids. *Physical Review B* **2009**, 79, 155107.
- (29) Liechtenstein, A. I., Anisimov, V. I. & Zaanen, J. Density-functional theory and strong interactions: Orbital ordering in Mott-Hubbard insulators *Physical Review B* **1995**, 52, R5467.
- (30) Ko, K. T.; Kim, K.; Kim, S. B.; Kim, H. D.; Kim, J. Y.; Min, B. I.; Park, J. H.; Chang, F. H.; Lin, H. J.; Tanaka, A.; Cheong, S. W. RKKY Frromagnetism with Ising-like Spin States in Intercalated $\text{Fe}_{1/4}\text{TaS}_2$. *Phys. Rev. Lett.* **2011**, 107, 247201.
- (31) Momma, K.; Izumi, F. VESTA 3 for Three-Dimensional Visualization of Crystal, Volumetric and Morphology Data. *J. Appl. Crystallogr.* **2011**, 44, 1272–1276.